Letter

Interlayer stacking controls the electronic properties of the van der Waals material 1*T*-TaS_2

Nelson Hua [1,2,*] Francesco Petocchi [3,4] Henry G. Bell [1,5] Gabriel Aeppli,[1,5,6] Philipp Werner [4,†] and Simon Gerber [1,‡]

[1]*PSI Center for Photon Science, Paul Scherrer Institute, 5232 Villigen PSI, Switzerland*
[2]*Institute for Quantum Electronics, ETH Zurich, 8093 Zurich, Switzerland*
[3]*Department of Quantum Matter Physics, University of Geneva, 1211 Geneva, Switzerland*
[4]*Department of Physics, University of Fribourg, 1700 Fribourg, Switzerland*
[5]*Laboratory for Solid State Physics and Quantum Center, ETH Zurich, 8093 Zurich, Switzerland*
[6]*Institute of Physics, EPF Lausanne, 1015 Lausanne, Switzerland*

(Received 31 March 2025; accepted 6 November 2025; published 3 March 2026)

Controlled stacking of van der Waals materials is a powerful tool for exploring the physics of quantum condensed matter. Given the small binding between layers, exploitation for engineering will require a breakthrough in stacking methodology or an ability to take advantage of thicker defective stacks. Here, we describe computational groundwork for the latter, using—on account of its promise for cold memory applications—1*T*-TaS_2 as a model system. Comparing recursive Hendricks-Teller calculations and Monte Carlo simulations to published x-ray diffraction data, we obtain the key parameters describing the random stacking in mesoscopic flakes. These then regulate the electronic structures via specification of the random stacks in dynamical mean-field theory simulations. Hubbard repulsion induces strongly correlated metallic, band, and Mott insulating layers, providing compelling evidence that electronic properties follow from the coexistence of more than the metallic and insulating planes associated with ordinary band theory.

DOI: 10.1103/6t8x-mbsd

Strong electronic correlations in single layers of van der Waals (vdW) materials can lead to intriguing properties not present in bulk counterparts [1,2]. Isolating such systems is possible due to the weak vdW interaction between layers that allows for exfoliation, providing stacking flexibility to construct heterostructures not feasible with other fabrication techniques [3]. However, even though the interlayer coupling is relatively weak, a particular stacking structure can still influence the emergent macroscopic properties. For example, the difference between AA and AB stacking in bilayer graphene significantly alters the range of band gap tunability [4,5]. Furthermore, the ability to twist bilayer graphene into a moiré pattern—where a magic angle leads to a flat band—opens pathways to unconventional superconductivity and correlated insulators [6,7]. Importantly, this sensitivity to stacking is also prevalent in other vdW materials such as $MoTe_2$ [8], CrX_3 (X = Br, I) [9], and WTe_2 [8,10], where the complex stacking in bulk is yet to be resolved. Understanding how particular stacking structures influence electronic properties is therefore a crucial step toward precise control and efficient heterostructure design [11,12].

A particular system for which there is both scientific and emerging technological interest related to stacking is the classic vdW material 1*T*-TaS_2, long known for its commensurate charge-density wave (CCDW) phase. Here, the discovery of a hidden, nonthermal metallic state [13] that can be switched either optically or electrically has provided a concept for memory devices [11,14,15], motivating considerable research that recently showed the switching to be a bulk effect associated with interlayer restacking [16,17]. Further progress in both the science and engineering aspects requires quantitative modeling of the stacking and its consequences for the electronic structure of the material, which are the topics of this Letter.

The various electronic phases of 1*T*-TaS_2, appearing as a function of temperature, are primarily characterized by the degree of *in-plane* commensurability of so-called polaron stars—motifs where 12 Ta atoms contract toward a central Ta atom (see Fig. 1). This has been confirmed through various experimental probes, such as transmission electron microscopy (TEM) [18,19], scanning tunneling microscopy (STM) [20–23], and x-ray diffraction (XRD) [16,17,24–26].

The *interlayer* coordination of the polaron stars can be described by T_a (dimer/bilayer), T_b, and T_c stacking (see Fig. 1). The exact distribution of stacking configurations in bulk 1*T*-TaS_2 remains undetermined as it is hidden to experimental techniques with limited subsurface sensitivity. TEM shows all three stacking configurations at the surface [19], while STM reveals predominantly T_a and T_c stacking with minority regions of T_b [27]. Since the exfoliation process is inherently invasive and the surface properties may deviate from those of the bulk, it is questionable to extrapolate these findings beyond the first few layers. Similarly, angle-resolved photoemission spectroscopy (ARPES) probes primarily the surface

*Contact author: nelson.hua@psi.ch
†Contact author: philipp.werner@unifr.ch
‡Contact author: simon.gerber@psi.ch

Published by the American Physical Society under the terms of the Creative Commons Attribution 4.0 International license. Further distribution of this work must maintain attribution to the author(s) and the published article's title, journal citation, and DOI.

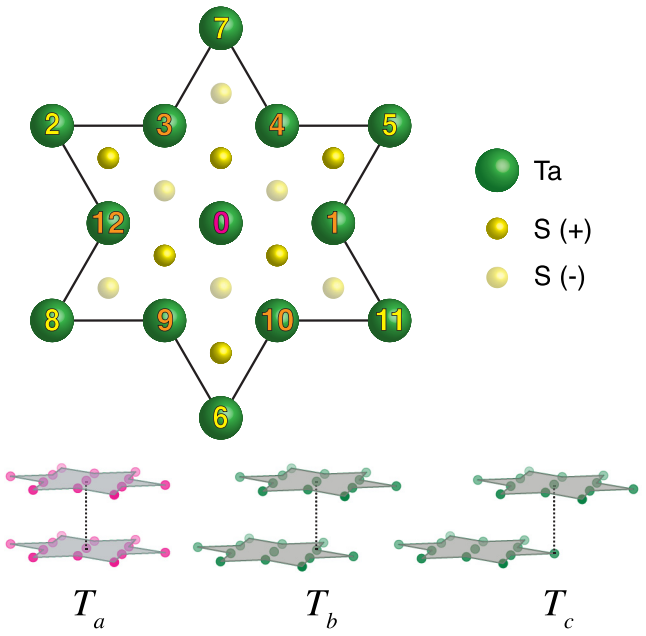

FIG. 1. Polaron star with Ta atoms indexed from 0 to 12. For T_a, T_b, and T_c configurations, the stacking of layers is referenced to the central Ta atom 0 (pink). The staggered S atoms above (+) and below (−) the Ta plane break the sixfold symmetry: T_b can be subdivided into T_{b1} and T_{b2} corresponding to stacking above Ta atoms {1, 3, 9} and {4, 10, 12} (orange), respectively. The same applies for T_{c1} and T_{c2} stacking above Ta atoms {2, 5, 6} and {7, 8, 11} (yellow), respectively.

for vacuum-ultraviolet light, and has thus far yielded conflicting results for the electronic ground state that is either band or Mott insulating [28–33]. When investigating coherent dynamics with time-resolved techniques [34–36], disagreements in the assignment of phonon modes persist. As demonstrated with density functional theory (DFT) calculations [37], the spectrum of phonon modes depends heavily on the exact stacking configuration. Several studies have also postulated monolayers buried within the bulk that host quantum spin liquids (QSLs) [38–41]. In contrast, other reports assumed predominant dimerization in the bulk [16,27,31,42,43], precluding a QSL phase.

Notwithstanding their variable outcomes, the studies mentioned above all conclude that the interlayer configuration mediates the emergent electronic properties of $1T$-TaS_2, underscoring the urgency to specify the stacking structure. The obvious method to determine the interlayer stacking order is XRD, due to its high penetration depth and resolution. However, despite several XRD experiments characterizing the Bragg peaks of the CCDW phase, a consensus has not been reached. Early studies [24,25] carefully mapped out the peak positions associated with the various CDW phases of $1T$-TaS_2. A disordered stacking was held accountable for the broad out-of-plane diffraction signals and half-ordered (dimer) peaks that are signatures of dimerization in the CCDW phase. But the exact stacking structure remained unspecified—though it was hypothesized that the CCDW phase is characterized by a distribution of T_a, T_b, and T_c stacking. In addition to the peak broadening indicative of disorder, CDW peaks at $l = \frac{1}{5}$ reciprocal lattice units (r.l.u.) [16,24,25,44] imply a periodicity of five layers that seems incompatible with the threefold CDW symmetry. Surprisingly, this unusual value has not been scrutinized and, to our best knowledge, no structure factor simulations are available to discern the exact stacking structure.

For the science and engineering of disordered systems, the key variables are the probabilities of particular configurations, which can then be used as inputs to model physical properties. Therefore, we start with Monte Carlo (MC) simulations and a recursive variation of the Hendricks-Teller (HT) method [45,46] with structure factor calculations to reveal the probabilities underpinning the random stacking of $1T$-TaS_2 seen experimentally. After demonstrating the equivalency of the numerical MC and analytical HT approaches, MC is used to generate multilayer configurations that reproduce the experimentally observed out-of-plane scattering pattern. Dynamical mean-field theory (DMFT) calculations of these configurations then provide access to the layer-resolved spectral functions of the bulk material and allow us to address open questions about the emergent behaviors, such as the controversy of whether the insulating low-temperature ground state is of Mott or band insulating nature. An advantage of the DMFT approach over simple DFT calculations is that it considers electron correlations that we identify as drivers for the formation of Mott insulating monolayers in the low-temperature ground state of $1T$-TaS_2.

XRD patterns from periodic structures can be calculated from the structure factor given by

$$F(\vec{Q}) = \sum_{i=1}^{M}\sum_{n=1}^{N} f_{i,n}(Q)e^{-i\vec{Q}\cdot\vec{R}_{i,n}}, \tag{1}$$

which is the sum of the atomic form factor f of all atoms in the unit cell $\vec{R}$. Here, the subscript i denotes the in-plane coordinate, while n is the out-of-plane position of the atoms. The scattered intensity is then obtained as $I(\vec{Q}) = |F(\vec{Q})|^2$. Assuming no in-plane disorder, we can define the structure factor for a monolayer $F_{\text{planar}}(\vec{Q})$ by

$$F_{\text{planar}}(\vec{Q}) = \sum_{i=1}^{M} f_i(Q)e^{-i\vec{Q}\cdot\vec{r}_i},$$

$$F(\vec{Q}) = F_{\text{planar}}(\vec{Q})\sum_{n=1}^{N} e^{-i\vec{Q}\cdot\Delta\vec{r}_n}, \tag{2}$$

where $\vec{R}_{i,n} = \vec{r}_i + \Delta\vec{r}_n$ is decomposed into its in- and out-of-plane components. This simplifies the calculation of layered systems, where $F_{\text{planar}}(\vec{Q})$ needs to be explicitly calculated only once, and the three-dimensional stacking structure is constructed by multiplying the sum of exponentials by the offset $\Delta\vec{r}_n$ of subsequent layers.

In the case of $1T$-TaS_2, there are 13 possible offsets corresponding to the T_a, T_b, and T_c stacking structures. With this formalism, we can exhaust all possible stacking distributions by varying the probabilities that follow $p_a + p_b + p_c = 1$. Due to the staggered S atoms that break the sixfold symmetry, p_b and p_c can be further decomposed into $p_{b1,b2}$ and $p_{c1,c2}$. Such simulations can be done numerically with MC methods (see the Supplemental Material [47]) or analytically with a

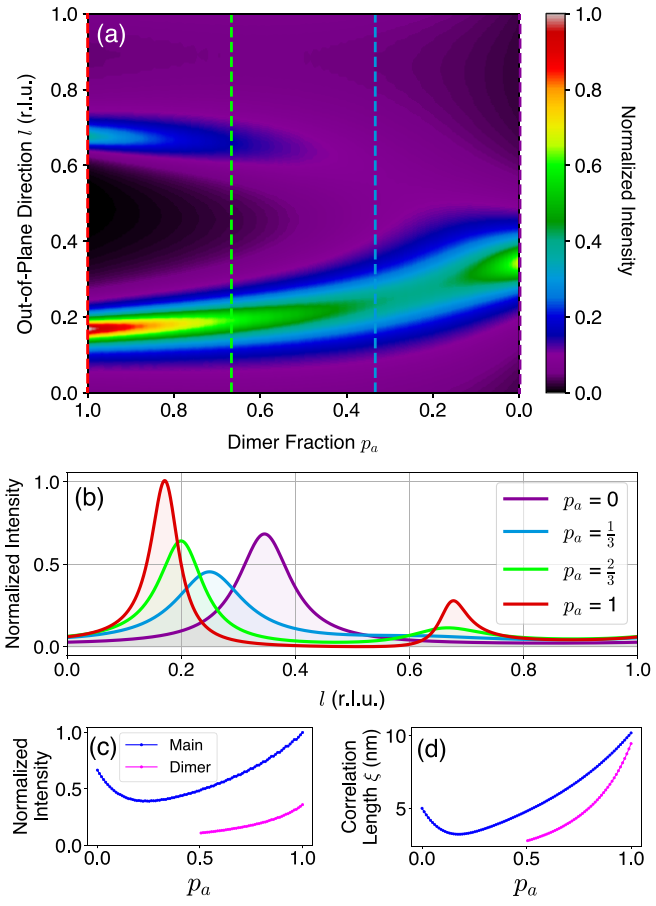

FIG. 2. (a) Simulated XRD intensity as a function of the out-of-plane reciprocal lattice direction l and the fraction of dimerized layers p_a for a system with T_c stacking. A half-ordered (dimer) peak appears when $p_a \gtrapprox 0.5$. (b) Selected line cuts from panel (a) showing how the main and dimer peaks evolve as a function of p_a. (c) Amplitude and (d) correlation length ξ of the peaks as a function of p_a.

recursive variation of the HT method suited for modeling disorder in one dimension [45,46]. For a system with N layers, the scattered intensity at a given $\vec{Q}$ position is described by

$$I(\vec{Q})/N = \vec{G}^* \cdot \vec{\psi} + \vec{G} \cdot \vec{\psi}^* - \vec{G}^* \cdot \vec{F}, \tag{3}$$

where the vector $G_i = g_i F_i$ and

$$\vec{\psi} = \frac{(I - T)^{-1}}{N}[(N+1)I - (I - T)^{-1}(I - T^{N+1})]\vec{F}.$$

I is the identity matrix. The complex transition matrix $T_{ij}(\vec{Q}) = A_{ij} e^{i\vec{Q}\cdot\Delta\vec{r}_{ij}}$ is determined by the stacking probabilities for layers of types i and j. g_i is a normalization factor to ensure the stacking probabilities sum to unity.

First, we calculate the XRD intensity $I(q_l)$ at fixed (q_h, q_k) matching the in-plane reciprocal space positions of the CCDW diffraction peaks for different stacking probability distributions. Here, we set $N = 100$ layers, corresponding to a typical flake thickness used in experiments of ≈60 nm, assuming a c-axis lattice constant of 0.59 nm [16,44,49,50]. Figure 2(a) shows $I(q_l)$ for T_c stacking and a distribution varying from all monolayers ($p_a = 0$) to a fully dimerized state ($p_a = 1$). Line cuts at selected p_a are shown in Fig. 2(b) and illustrate how

TABLE I. Out-of-plane CCDW Bragg peak positions from previous x-ray diffraction studies and the corresponding material fraction that is dimerized according to our HT model.

Experiment	l (r.l.u.)	Corresponding dimer fraction p_a
Laulhé *et al.* [44]	0.20	0.66
Stahl *et al.* [16]	0.20	0.66
Tanda *et al.* [24]	0.18	0.84
Ritschel *et al.* [31]	0.18	0.84
Nicholson *et al.* [48]	0.18	0.84

the main and dimer peaks evolve as a function of the degree of dimerization. Complete dimerization with T_c stacking results in a main peak position at $l = \frac{1}{6}$ r.l.u. This is not consistent with XRD experiments and indicates that the CCDW state of $1T$-TaS_2 is not fully dimerized. Comparing with the peak positions found in XRD experiments (see Table I), we can estimate the fraction of dimers in the system: The five-layer periodicity from $l \approx \frac{1}{5}$ r.l.u originates from $p_a \approx \frac{2}{3}$, corresponding to an average distribution of two dimerized layers to one monolayer. We also conclude that the bulk cannot contain significant T_b stacking as the calculated diffraction would deviate further from the experiments (see the Supplemental Material [47]).

Next, we perform DMFT calculations on ten representative structures, each with a thickness of 20 layers, that follow a dimer-to-monolayer distribution of 2:1 and T_c stacking. For each structure, we construct a low-energy Hamiltonian H with a single orbital per layer. This orbital corresponds to the half-filled band with d_{z^2} character that emerges in the low-temperature CCDW phase and is localized on the Ta site at the center of each polaron star [43,51]. The standard procedure to obtain H involves performing DFT calculations for the desired lattice structure and projecting the resulting Kohn-Sham band structure onto a set of localized Wannier states with defined orbital character. This projection enables a tight-binding parametrization of the effective Hamiltonian. However, the computational cost increases rapidly with the number of sites in the unit cell, which would include 780 atoms for our setup. We therefore adopt a simpler, though well-motivated procedure: The effective single-band tight-binding Hamiltonian for the nth isolated monolayer is calculated by DFT, whereas the real-space structure of the hoppings between layers is determined by the stacking arrangement of the adjacent layers. Since one effective orbital is associated with each polaron star, a single hopping parameter t_v, connecting the polarons on neighboring layers, is sufficient to account for the stacking arrangement. This procedure was previously employed, where the values $t_v = 0.2$ eV for T_a and $t_v = 0.048$ eV for T_c stacking were obtained by optimizing against experimental data, specifically ARPES [48] and STM [52] measurements. While this minimal model may not describe all details of the multilayer system's electronic structure, it qualitatively captures how the kinetic energy is affected by the specific stacking arrangement. Importantly, our modeling reproduces the hybridization gap associated with the T_a configuration already in the absence of correlations (see the dashed layer-resolved spectra in Fig. 3). In the simulations, we use a Hubbard

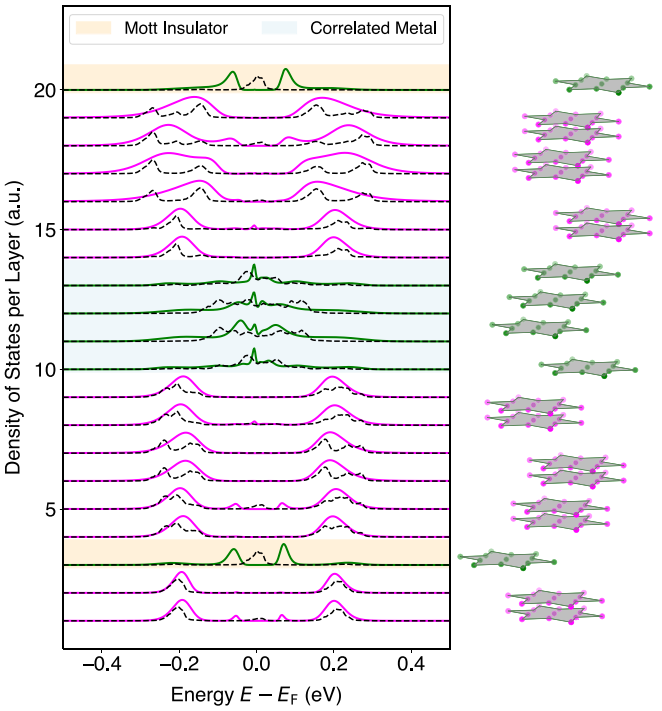

FIG. 3. Black dashed lines correspond to the layer-resolved density of states (DOS), while green and pink lines depict the corresponding monolayer and dimer local spectral function $A_n(\omega)$, respectively, calculated from DMFT for an exemplary 20-layer $1T$-TaS_2 system. Except for the dimers (T_a), the stacking between the layers is all T_c. The ∼0.4 eV wide gap, present already at the noninteracting level, stems from the strong hybridization of T_a stacked layers. Mott insulating and correlated metallic layers are marked in yellow and green, respectively, while the unshaded layers are band insulating.

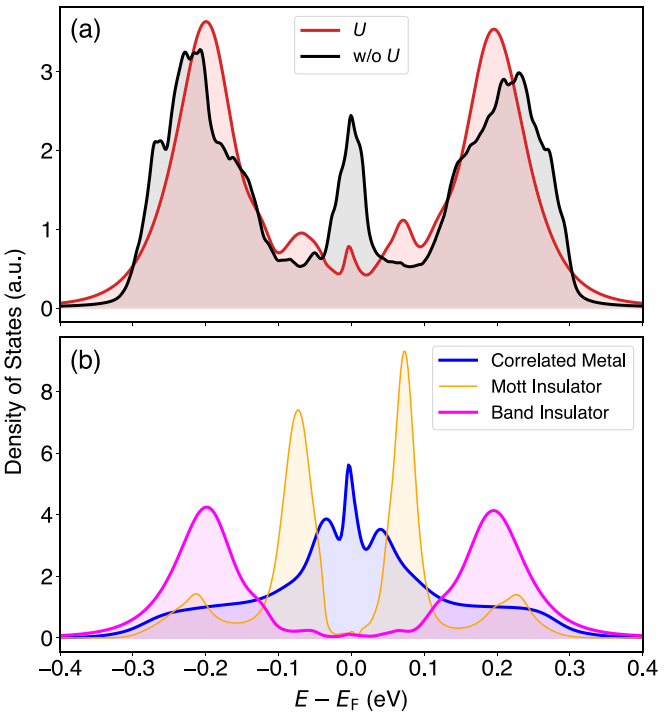

FIG. 4. (a) Average spectral function $A(\omega)$ from ten 20-layer $1T$-TaS_2 systems with and without the local Hubbard U interaction term. (b) Based on the low-frequency behavior of the self-energy for each layer in the ten 20-layer systems, $A_n(\omega)$ is averaged over the corresponding metallic (24 layers), Mott insulating (14 layers), and band insulating (162 layers) insulating states.

repulsion of $U = 0.2$ eV [48,52] and account for local electronic correlations with a real-space extension of DMFT that provides an independent local self-energy for the nth layer. All DMFT calculations are performed assuming $T \sim 30$ K and a half-filled system. Layer-resolved spectral functions $A_n(\omega)$ are obtained with the maximum entropy method. We use open boundary conditions in the stacking direction, so the external layers are representative of surface states.

Correlation effects are small in dimerized layers, as can be seen from the pink curves in Fig. 3, which resemble the noninteracting results in black. The situation is different for nondimerized layers connected by T_c stacking. In the case of monolayers surrounded exclusively by dimers, we observe a gap in the spectrum only when using DMFT, i.e., when electron correlations are considered, and the diverging self-energy at low Matsubara frequencies demonstrates the Mott insulating nature of the state (yellow shading). On the other hand, when stackings different from T_a occur across a couple of layers, a strongly correlated metallic state emerges within the bulk (green shading).

Taking all ten configurations into account (see Fig. S6 of the Supplemental Material [47] for the remaining configurations), we compute the quantity most relevant for electrical transport in devices [13,17], namely, the average spectral function $A(\omega)$, shown in Fig. 4(a). While the quasiparticle peak of the noninteracting DOS (black) is suppressed when accounting for U and a noticeable ∼0.4 eV gap is present (red), finite spectral weight remains at the Fermi energy E_F. By analyzing the divergence of the self-energy, we categorize the layers by their electronic behaviors: Correlated metal, as well as Mott and band insulators. The spectral functions for these states are shown in Fig. 4(b), revealing that the nonzero spectral weight at E_F is due to the presence of the correlated metallic layers. Thus, we find that all dimerized layers are band insulating. Isolated monolayers tend to be Mott insulating while consecutive monolayers are metallic, although the precise local configuration matters (see the Supplemental Material [47]).

In summary, we employed a recursive variation of the HT method [45,46] to exhaust the phase space of possible stacking configurations, including the degree of dimerization. Inputting these configurations into structure factor calculations to simulate the x-ray diffraction intensities, we concluded that the low-temperature, "insulating" CCDW state of $1T$-TaS_2 is dominated by T_c stacking and a mix of T_a-stacked dimers and monolayers in a ratio of ≈2 : 1. The dimers are band insulating, and—from our DMFT calculations—the monolayers behave as strongly correlated metals or Mott insulators depending upon their stacking neighborhood. Earlier studies suggested that the cooling rate to the CCDW state can affect the degree of dimerization [26,43] and, hence, the material's electronic properties. Our results substantiate this

possibility based on the variation of the out-of-plane CCDW diffraction peak position observed in different XRD experiments [16,17,31,44,48]. Furthermore, the confirmation of buried Mott insulating monolayers identifies hosts for possible QSL states [39–41,53] in this stacked two-dimensional material. The formalism we present here is therefore a powerful tool that connects XRD data to the real-space interlayer stacking structure, and which can be extended to other equilibrium and nonequilibrium phases of $1T$-TaS_2 (see Appendices A–C), as well as a wider range of vdW materials [54–56] with different stacking configurations.

Our DMFT calculations revealed the coexistence of correlated metallic, as well as both band and Mott insulating layers in $1T$-TaS_2, which is supported by experimental evidence of correlated metallic [27,52], Mott [20,27,33,57], and band insulating [20,27,32,33,52] states seen by surface-sensitive techniques such as ARPES and STM. The coexistence of the three phases along the stacking direction explains these contradictory experimental findings, where the surface state depends on which layer is revealed through the exfoliation process. Through this reconciliation, we also demonstrated how interlayer hopping together with on-site Coulomb interactions controls the electronic properties of randomly stacked vdW materials. While fixed heterostructures with gates and moiré or translated layers have provided very fertile ground for the study of many-body physics, thick vdW flakes of a single material represent a more accessible starting point for *in situ* tuning of the stacking, e.g., by thermal protocols or weak electrical and optical pulses. This approach has recently been explored to access nonequilibrium states for not only $1T$-TaS_2 but also other vdW systems, such as $EuTe_4$ [56], or to introduce interlayer sliding for ferroelectric polarization control [58–61]. The averaging implicit for thicker flakes should lead to greater reproducibility, and therefore greater application potential, for the random stacks characteristic of vdW materials. The combination of the HT method with DMFT calculations introduced here represents a significant advance as it provides a framework to account for the structural and electronic behaviors associated with exactly such stacks.

Acknowledgments. We acknowledge fruitful discussions with D. Mihailovic. This research was funded by the Swiss National Science Foundation and the Slovenian Research and Innovation Agency as a part of the WEAVE framework (Grant No. 213148). G.A. acknowledges funding from the European Research Council under the European Union's Horizon 2020 Research and Innovation Programme, within Grant Agreement No. 810451 (HERO).

Data availability. The data that support the findings of this article are openly available [62].

Appendix A: Probing stacking dynamics with coherent x-rays. Beyond replicating the XRD signals originating from the static CCDW stacking structure, the numerical MC and analytical HT formalisms have implications for the ability to directly visualize stacking dynamics in a coherent x-ray scattering experiment. Figure 5 shows the intensity of a CCDW diffraction peak generated via the HT approach, and averages of N configurations produced by the stochastic MC method. Averaging $N \to \infty$ configurations from MC reproduces the HT solution, demonstrating their equivalence. This is quantified in the inset of Fig. 5. For the case $N = 1$, the residual

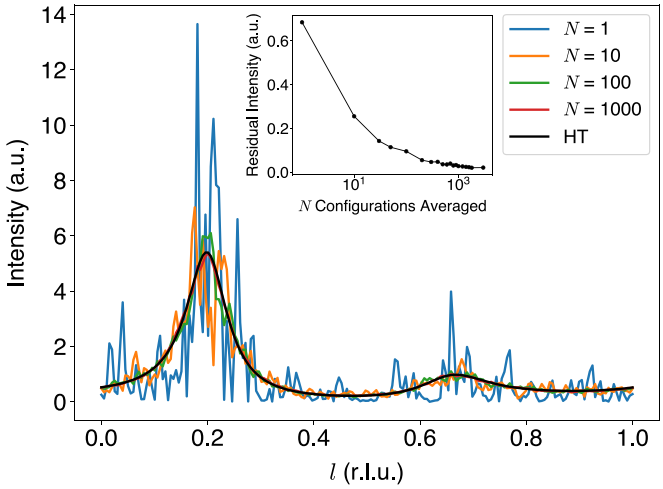

FIG. 5. Simulated XRD signal along the (0.308, −0.077, l) direction in reciprocal space of a 100-layer $1T$-TaS_2 stacking configuration with a dimer-to-monolayer ratio of 2:1. The analytical HT solution (black) is overlaid with the results from averaging N configurations generated by the MC method. The inset shows the intensity differences between the HT result and MC signals from N averaged configurations.

intensity between the two formalisms shows a large variance with points of zero intensity. Here, the stacking structure effectively acts as a diffraction grating for a coherent x-ray beam with a small spot size that produces a speckle pattern. The MC method can therefore be used to simulate the CCDW diffraction pattern generated by partially and fully coherent x-rays, where stacking dynamics manifests as a fluctuating speckle pattern.

Appendix B: Stacking order of the nearly commensurate and hidden CDW states of $1T$-TaS_2. Disordered stacking is simulated by assuming that the stacking probabilities within a symmetry group are equal. For example, in the T_{c1} group, the stackings of Ta atoms {7, 8, 11} above the central Ta atom are all equally likely. In this manner, we can exhaust all possible disordered stacking distributions. Ordered stacking structures and the degree of order can also be simulated with the HT and MC formalisms. Several ordered stacking structures in $1T$-TaS_2 have previously been proposed [63]. Figure 6 shows two possibilities, corresponding to a linear and a spiral staircase T_c stacking order. A thorough description of the mathematical formalism for simulating the stacking order is presented in the Supplemental Material [47].

The simulated stacking can be compared to the experimental Bragg peak positions of the nearly-commensurate and the nonthermal hidden charge-density wave (NCCDW and HCDW) phases of $1T$-TaS_2 [16]. Figures 6(a) and 6(b) show the out-of-plane XRD intensity from a linear staircase stacking, where the vertical dotted lines denote the $l = \pm\frac{1}{3}$ locations of the HCDW and NCCDW peaks. Due to the S atoms that break the sixfold symmetry (see Fig. 1), two in-plane CDW coordinates are shown to capture the symmetry breaking. Clearly, this stacking does not describe those CDW phases, while the spiral staircase stacking structure in Fig. 6(c) and 6(d) yields diffraction patterns that align with the experiments. Here, p_2 describes the degree of ordered stacking,

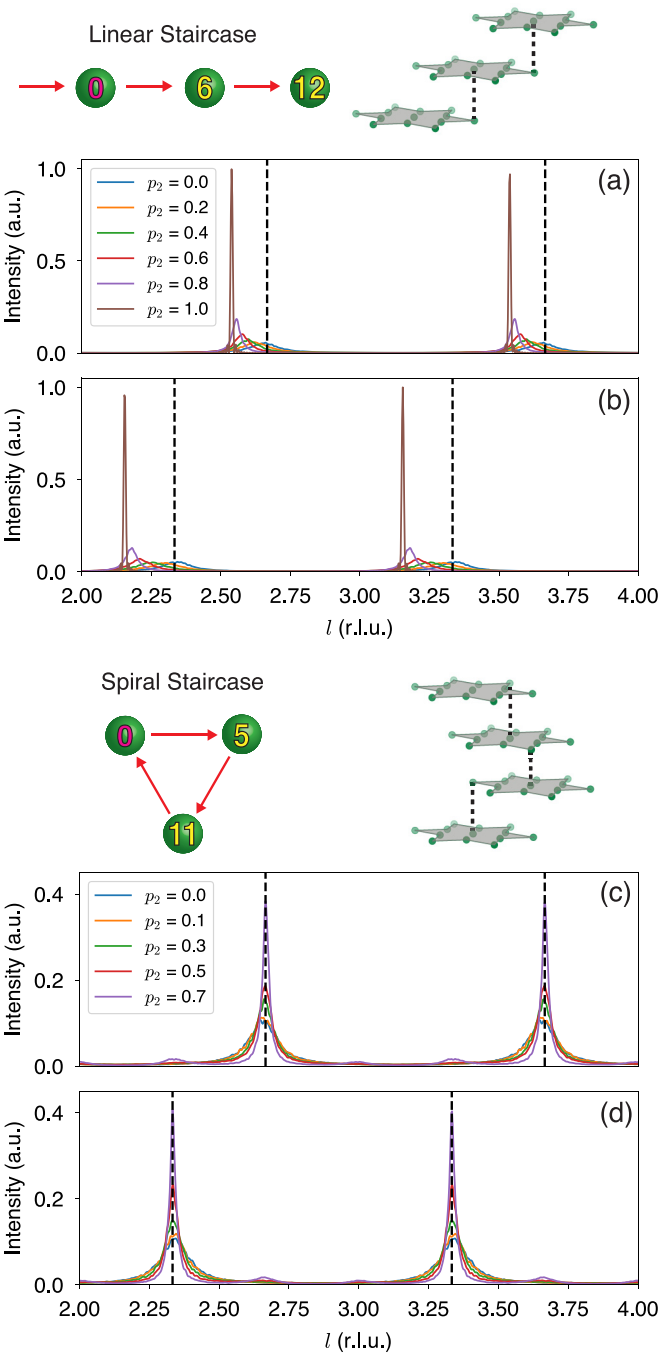

FIG. 6. A linear and a spiral staircase stacking are schematically shown on the top and middle, respectively. Ta atoms are numbered as in Fig. 1 and refer to the stacking order. The XRD intensity is shown along (a), (c) (0.077, 0.231, l) and (b), (d) (0.308, −0.077, l), corresponding to the two symmetry equivalent groups described in Fig. 1, and as a function of the order p_2. The vertical dotted lines refer to the l positions where the NCCDW and HCDW peaks appear in experiments.

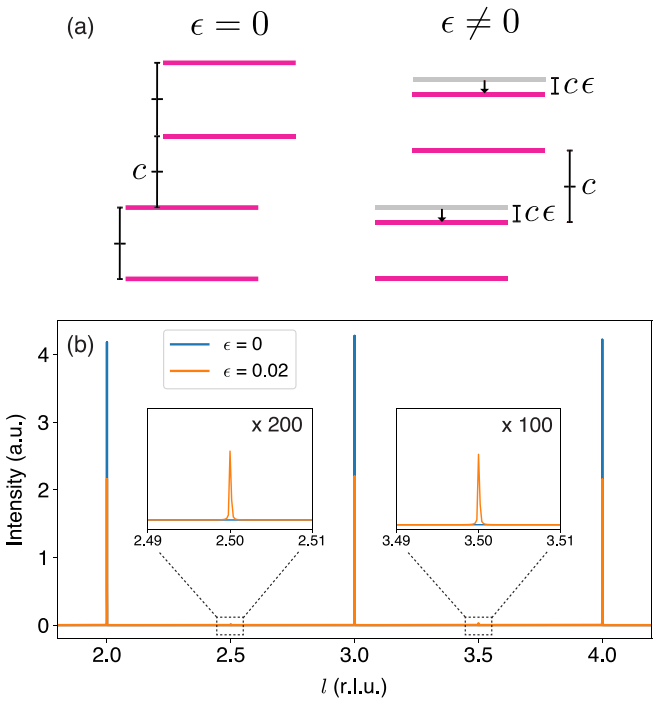

FIG. 7. (a) Schematic of two T_c-stacked dimers with identical intradimer and interdimer distances (left, $\epsilon = 0$) and an intradimer contraction (right, $\epsilon \neq 0$). (b) Simulated (0, 0, l) lattice peak intensity, where weak half-ordered superlattice signals appear in the contracted case ($\epsilon = 0.02$).

corresponding to the length scale before a stacking fault is introduced. Although the interlayer correlation length of the NCCDW and HCDW phases is larger than that of the CCDW phase [16], there is no experimental evidence for additional out-of-plane superlattice signals, e.g., originating from dimers, in those phases. However, additional peaks appear in Figs. 6(c) and 6(d) when $p_2 \gtrsim 0.7$. Based on the peak location and intensity distribution along the out-of-plane l direction, we therefore assign a spiral staircase ordered stacking with $p_2 \approx 0.6$ for the NCCDW and HCDW states.

Appendix C: Out-of-plane dimer contraction. XRD directly reveals the presence of dimers in the CCDW phase via half-ordered CDW peaks [16,17,24]. In addition, an overall out-of-plane lattice contraction, estimated to be 0.43%, is observed proceeding from the NCCDW phase to the low-temperature CCDW state [32]. What remains to be investigated is whether the intradimer distance (T_a) and the distance between dimers/monolayers (T_c) are the same or not. We use the HT formalism to look into this question by introducing the parameter ϵ, defined as the fraction of the c lattice constant that a dimer contracts in the CCDW phase. As shown in Fig. 7(a), the separation between dimerized layers changes from c to $(1-\epsilon)c$, whereas the distance between the two dimerized pairs remains c. This parametrization allows for a different lattice spacing between dimers, pairs of dimers, and monolayers and dimers. A detailed calculation is presented in the Supplemental Material [47], but setting $\epsilon = 0.02$ and calculating lattice diffraction peaks along the out-of-plane (0, 0, l) direction, we find half-ordered lattice diffraction peaks, in line with XRD experiments [17,32]. The relative intensities of the half-ordered peaks from our simulations are about a magnitude larger than seen experimentally, implying $\epsilon \ll 0.02$.

[1] Z. Fei, T. Palomaki, S. Wu, W. Zhao, X. Cai, B. Sun, P. Nguyen, J. Finney, X. Xu, and D. H. Cobden, Edge conduction in monolayer WTe_2, Nat. Phys. **13**, 677 (2017).

[2] X. Qian, J. Liu, L. Fu, and J. Li, Quantum spin Hall effect in two-dimensional transition metal dichalcogenides, Science **346**, 1344 (2014).

[3] A. K. Geim and I. V. Grigorieva, Van der Waals heterostructures, Nature (London) **499**, 419 (2013).

[4] M. L. Ould NE, M. Boujnah, A. Benyoussef, and A. El Kenz, Electronic and electrical conductivity of AB and AA-stacked bilayer graphene with tunable layer separation, J. Supercond. Novel Magn. **30**, 1263 (2017).

[5] X. Liang, Z. A. H. Goodwin, V. Vitale, F. Corsetti, A. A. Mostofi, and J. Lischner, Effect of bilayer stacking on the atomic and electronic structure of twisted double bilayer graphene, Phys. Rev. B **102**, 155146 (2020).

[6] R. Bistritzer and A. H. MacDonald, Moiré bands in twisted double-layer graphene, Proc. Natl. Acad. Sci. USA **108**, 12233 (2011).

[7] Y. Cao, V. Fatemi, S. Fang, K. Watanabe, T. Taniguchi, E. Kaxiras, and P. Jarillo-Herrero, Unconventional superconductivity in magic-angle graphene superlattices, Nature (London) **556**, 43 (2018).

[8] J. L. Hart, *et al.*, Emergent layer stacking arrangements in *c*-axis confined $MoTe_2$, Nat. Commun. **14**, 4803 (2023).

[9] M. Jang, *et al.*, Direct observation of twisted stacking domains in the van der Waals magnet $CrIi_3$, Nat. Commun. **15**, 5925 (2024).

[10] S. Ji, O. Grånäs, and J. Weissenrieder, Manipulation of stacking order in *Td*-WTe_2 by ultrafast optical excitation, ACS Nano **15**, 8826 (2021).

[11] Y. Liu, N. O. Weiss, X. Duan, H.-C. Cheng, Y. Huang, and X. Duan, Van der Waals heterostructures and devices, Nat. Rev. Mater. **1**, 16042 (2016).

[12] W. Wang, B. Zhao, X. Ming, and C. Si, Multiple quantum states induced in 1*T*-$TaSe_2$ by controlling the stacking order of charge density waves, Adv. Funct. Mater. **33**, 2214583 (2023).

[13] L. Stojchevska, I. Vaskivskyi, T. Mertelj, P. Kusar, D. Svetin, S. Brazovskii, and D. Mihailovic, Ultrafast switching to a stable hidden quantum state in an electronic crystal, Science **344**, 177 (2014).

[14] Q. H. Wang, K. Kalantar-Zadeh, A. Kis, J. N. Coleman, and M. S. Strano, Electronics and optoelectronics of two-dimensional transition metal dichalcogenides, Nat. Nanotechnol. **7**, 699 (2012).

[15] D. Jariwala, V. K. Sangwan, L. J. Lauhon, T. J. Marks, and M. C. Hersam, Emerging device applications for semiconducting two-dimensional transition metal dichalcogenides, ACS Nano **8**, 1102 (2014).

[16] Q. Stahl, M. Kusch, F. Heinsch, G. Garbarino, N. Kretzschmar, K. Hanff, K. Rossnagel, J. Geck, and T. Ritschel, Collapse of layer dimerization in the photo-induced hidden state of 1*T*-TaS_2, Nat. Commun. **11**, 1247 (2020).

[17] C. Burri, *et al.*, Imaging of electrically controlled van der Waals layer stacking in 1*T*-TaS_2, Nat. Commun. **16**, 10296 (2025).

[18] A. W. Tsen, *et al.*, Structure and control of charge density waves in two-dimensional 1*T*-TaS_2, Proc. Natl. Acad. Sci. USA **112**, 15054 (2015).

[19] G. Wang, X. Yu, E. Zhao, D. Li, L. Wang, and J. Lin, Atomic visualization of the 3D charge density wave stacking in 1*T*-TaS_2 by cryogenic transmission electron microscopy, Nano Lett. **23**, 4318 (2023).

[20] H. Yang, B. Lee, J. Bang, S. Kim, D. Wulferding, S.-H. Lee, and D. Cho, Origin of distinct insulating domains in the layered charge density wave material 1*T*-TaS_2, Adv. Sci. **11**, 2401348 (2024).

[21] L. Ma, *et al.*, A metallic mosaic phase and the origin of Mott-insulating state in 1*T*-TaS_2, Nat. Commun. **7**, 10956 (2016).

[22] Y. A. Gerasimenko, P. Karpov, I. Vaskivskyi, S. Brazovskii, and D. Mihailovic, Intertwined chiral charge orders and topological stabilization of the light-induced state of a prototypical transition metal dichalcogenide, npj Quantum Mater. **4**, 32 (2019).

[23] J. Ravnik, M. Diego, Y. Gerasimenko, Y. Vaskivskyi, I. Vaskivskyi, T. Mertelj, J. Vodeb, and D. Mihailovic, A time-domain phase diagram of metastable states in a charge ordered quantum material, Nat. Commun. **12**, 2323 (2021).

[24] S. Tanda, T. Sambongi, T. Tani, and S. Tanaka, X-ray study of charge density wave structure in 1*T*-TaS_2, J. Phys. Soc. Jpn. **53**, 476 (1984).

[25] K. Nakanishi and H. Shiba, Theory of three-dimensional orderings of charge-density waves in 1*T*-TaX_2 (X: S, Se), J. Phys. Soc. Jpn. **53**, 1103 (1984).

[26] A. de la Torre, *et al.*, Dynamic phase transition in 1*T*-TaS_2 via a thermal quench, Nat. Phys. **21**, 1267 (2025).

[27] C. J. Butler, M. Yoshida, T. Hanaguri, and Y. Iwasa, Mottness versus unit-cell doubling as the driver of the insulating state in 1*T*-TaS_2, Nat. Commun. **11**, 2477 (2020).

[28] L. Perfetti, P. A. Loukakos, M. Lisowski, U. Bovensiepen, H. Berger, S. Biermann, P. S. Cornaglia, A. Georges, and M. Wolf, Time evolution of the electronic structure of 1*T*-TaS_2 through the insulator-metal transition, Phys. Rev. Lett. **97**, 067402 (2006).

[29] S. Hellmann, *et al.*, Ultrafast melting of a charge-density wave in the Mott insulator 1*T*-TaS_2, Phys. Rev. Lett. **105**, 187401 (2010).

[30] S. Hellmann, *et al.*, Time-domain classification of charge-density-wave insulators, Nat. Commun. **3**, 1069 (2012).

[31] T. Ritschel, J. Trinckauf, K. Koepernik, B. Büchner, M. v. Zimmermann, H. Berger, Y. I. Joe, P. Abbamonte, and J. Geck, Orbital textures and charge density waves in transition metal dichalcogenides, Nat. Phys. **11**, 328 (2015).

[32] Y. D. Wang, W. L. Yao, Z. M. Xin, T. T. Han, Z. G. Wang, L. Chen, C. Cai, Y. Li, and Y. Zhang, Band insulator to Mott insulator transition in 1*T*-TaS_2, Nat. Commun. **11**, 4215 (2020).

[33] Y. Wang, *et al.*, Dualistic insulator states in 1*T*-TaS_2 crystals, Nat. Commun. **15**, 3425 (2024).

[34] Y. Toda, K. Tateishi, and S. Tanda, Anomalous coherent phonon oscillations in the commensurate phase of the quasi-two-dimensional 1*T*-TaS_2 compound, Phys. Rev. B **70**, 033106 (2004).

[35] J. Ravnik, I. Vaskivskyi, T. Mertelj, and D. Mihailovic, Real-time observation of the coherent transition to a metastable emergent state in 1*T*-TaS_2, Phys. Rev. B **97**, 075304 (2018).

[36] K. Tanimura, Photoinduced discommensuration of the commensurate charge-density wave phase in 1*T*-TaS_2, Phys. Rev. B **97**, 245115 (2018).

[37] O. R. Albertini, R. Zhao, R. L. McCann, S. Feng, M. Terrones, J. K. Freericks, J. A. Robinson, and A. Y. Liu, Zone-center phonons of bulk, few-layer, and monolayer 1*T*-TaS_2: Detection

of commensurate charge density wave phase through Raman scattering, Phys. Rev. B **93**, 214109 (2016).
[38] M. Klanjšek, A. Zorko, R. Žitko, J. Mravlje, Z. Jagličić, P. K. Biswas, P. Prelovšek, D. Mihailovic, and D. Arčon, A high-temperature quantum spin liquid with polaron spins, Nat. Phys. **13**, 1130 (2017).
[39] K. T. Law and P. A. Lee, $1T$-TaS_2 as a quantum spin liquid, Proc. Natl. Acad. Sci. USA **114**, 6996 (2017).
[40] M. Kratochvilova, A. D. Hillier, A. R. Wildes, L. Wang, S.-W. Cheong, and J.-G. Park, The low-temperature highly correlated quantum phase in the charge-density-wave $1T$-TaS_2 compound, npj Quantum Mater. **2**, 42 (2017).
[41] S. Mañas-Valero, B. M. Huddart, T. Lancaster, E. Coronado, and F. L. Pratt, Quantum phases and spin liquid properties of $1T$-TaS_2, npj Quantum Mater. **6**, 69 (2021).
[42] T. Ritschel, H. Berger, and J. Geck, Stacking-driven gap formation in layered $1T$-TaS_2, Phys. Rev. B **98**, 195134 (2018).
[43] S.-H. Lee, J. S. Goh, and D. Cho, Origin of the insulating phase and first-order metal-insulator transition in $1T$-TaS_2, Phys. Rev. Lett. **122**, 106404 (2019).
[44] C. Laulhé, *et al.*, X-ray study of femtosecond structural dynamics in the 2D charge density wave compound $1T$-TaS_2, Physica B: Condens. Matter **460**, 100 (2015).
[45] S. B. Hendricks and E. Teller, X-ray interference in partially ordered layer lattices, J. Chem. Phys. **10**, 147 (1942).
[46] M. M. J. Treacy, J. M. Newsam, and M. W. Deem, A general recursion method for calculating diffracted intensities from crystals containing planar faults, Proc. R. Soc. London A **433**, 499 (1991).
[47] See Supplemental Material at http://link.aps.org/supplemental/10.1103/6t8x-mbsd for a description of the structure factor calculations, the symmetry of the polaron stars, the Hendricks-Teller model and the Monte Carlo simulations, which also includes Refs. [64–66].
[48] C. W. Nicholson, F. Petocchi, B. Salzmann, C. Witteveen, M. Rumo, G. Kremer, O. Ivashko, F. O. von Rohr, P. Werner, and C. Monney, Gap collapse and flat band induced by uniaxial strain in $1T$-TaS_2, Phys. Rev. B **109**, 035167 (2024).
[49] Y. Yu, *et al.*, Gate-tunable phase transitions in thin flakes of $1T$-TaS_2, Nat. Nanotechnol. **10**, 270 (2015).
[50] M. Yoshida, R. Suzuki, Y. Zhang, M. Nakano, and Y. Iwasa, Memristive phase switching in two-dimensional $1T$-TaS_2 crystals, Sci. Adv. **1**, e1500606 (2015).
[51] X.-L. Yu, D. Y. Liu, Y. M. Quan, J. Wu, H. Q. Lin, K. Chang, and L. J. Zou, Electronic correlation effects and orbital density wave in the layered compound $1T$-TaS_2, Phys. Rev. B **96**, 125138 (2017).
[52] F. Petocchi, C. W. Nicholson, B. Salzmann, D. Pasquier, O. V. Yazyev, C. Monney, and P. Werner, Mott versus hybridization gap in the low-temperature phase of $1T$-TaS_2, Phys. Rev. Lett. **129**, 016402 (2022).
[53] E. S. Bozin, M. Abeykoon, S. Conradson, G. Baldinozzi, P. Sutar, and D. Mihailovic, Crystallization of polarons through charge and spin ordering transitions in $1T$-TaS_2, Nat. Commun. **14**, 7055 (2023).
[54] Z. Ren, *et al.*, Plethora of tunable Weyl fermions in kagome magnet Fe_3Sn_2 thin films, npj Quantum Mater. **7**, 109 (2022).
[55] S. A. Ekahana, *et al.*, Anomalous electrons in a metallic kagome ferromagnet, Nature (London) **627**, 67 (2024).
[56] R. Venturini, M. Rupnik, J. Gašperlin, J. Lipič, P. Šutar, Y. Vaskivskyi, F. Ščepanović, D. Grabnar, D. Golež, and D. Mihailovic, Electrically driven non-volatile resistance switching between charge density wave states at room temperature, arXiv:2412.13094.
[57] J. C. Petersen, *et al.*, Clocking the melting transition of charge and lattice order in $1T$-TaS_2 with ultrafast extreme-ultraviolet angle-resolved photoemission spectroscopy, Phys. Rev. Lett. **107**, 177402 (2011).
[58] M. Wu and J. Li, Sliding ferroelectricity in 2D van der Waals materials: Related physics and future opportunities, Proc. Natl. Acad. Sci. USA **118**, e2115703118 (2021).
[59] R. Bian, *et al.*, Developing fatigue-resistant ferroelectrics using interlayer sliding switching, Science **385**, 57 (2024).
[60] K. Yasuda, E. Zalys-Geller, X. Wang, D. Bennett, S. S. Cheema, K. Watanabe, T. Taniguchi, E. Kaxiras, P. Jarillo-Herrero, and R. Ashoori, Ultrafast high-endurance memory based on sliding ferroelectrics, Science **385**, 53 (2024).
[61] M. Vizner Stern, S. Salleh Atri, and M. Ben Shalom, Sliding van der Waals polytypes, Nat. Rev. Phys. **7**, 50 (2025).
[62] N. Hua, Interlayer stacking controls the electronic properties of the van der Waals material $1T$-TaS_2 (2025), https://zenodo.org/records/18657906.
[63] M. B. Walker and R. L. Withers, Stacking of charge-density waves in $1T$ transition-metal dichalcogenides, Phys. Rev. B **28**, 2766 (1983).
[64] R. Brouwer and F. Jellinek, The low-temperature superstructures of $1T$-$TaSe_2$ and $2H$-$TaSe_2$, Physica B+C **99**, 51 (1980).
[65] A. Zong, *et al.*, Ultrafast manipulation of mirror domain walls in a charge density wave, Sci. Adv. **4**, eaau5501 (2018).
[66] D. Frenkel, K. J. Schrenk, and S. Martiniani, Monte Carlo sampling for stochastic weight functions, Proc. Natl. Acad. Sci. USA **114**, 6924 (2017).